Polarization alignment, phase transition, and piezoelectricity development in polycrystalline $0.5Ba(Zr_{0.2}Ti_{0.8})O_3$-$0.5(Ba_{0.7}Ca_{0.3})TiO_3$

Hanzheng Guo,[1] Brian K. Voas,[1] Shujun Zhang,[2] Chao Zhou,[3] Xiaobing Ren,[3] Scott P. Beckman,[1] and Xiaoli Tan[1,*]

[1]*Department of Materials Science and Engineering, Iowa State University, Ames, Iowa 50011, USA*

[2]*Materials Research Institute, Pennsylvania State University, University Park, Pennsylvania 16802, USA*

[3]*Multi-disciplinary Materials Research Center, Frontier Institute of Science and Technology, Xi'an Jiaotong University, Xi'an 710049, China*

(Received 11 March 2014; revised manuscript received 22 May 2014; published 14 July 2014)

The microstructural origin of the exceptionally high piezoelectric response of polycrystalline $0.5Ba(Zr_{0.2}Ti_{0.8})O_3$-$0.5(Ba_{0.7}Ca_{0.3})TiO_3$ is investigated using *in situ* transmission electron microscopy, in addition to a wide variety of bulk measurements and first-principles calculations. A direct correlation is established relating a domain wall-free state to the ultrahigh piezoelectric d_{33} coefficient in this $BaTiO_3$-based composition. The results suggest that the unique single-domain state formed during electrical poling is a result of a structural transition from coexistent rhombohedral and tetragonal phases to an orthorhombic phase that has an anomalously low elastic modulus. First-principles calculations indicate that incorporating Ca^{2+} and Zr^{4+} into $BaTiO_3$ reduces the differences in structure and energy of the variant perovskite phases, and $0.5Ba(Zr_{0.2}Ti_{0.8})O_3$-$0.5(Ba_{0.7}Ca_{0.3})TiO_3$ is identified as unique because the variant phases become almost indistinguishable. The structural instability and elastic softening observed here are responsible for the excellent piezoelectric properties of this lead-free ceramic.

DOI: 10.1103/PhysRevB.90.014103 PACS number(s): 77.80.Dj, 68.37.Lp, 77.65.−j, 77.84.Cg

I. INTRODUCTION

Lead-free piezoelectric ceramics have received tremendous attention worldwide in the past decade due to environmental concerns over the toxicity of lead in $Pb(Zr,Ti)O_3$-based compositions, which have been the mainstay for high-performance actuators and transducers for over half a century owing to their superior electromechanical properties [1,2]. Among the most studied lead-free solid solutions, $Ba(Zr_{0.2}Ti_{0.8})O_3$-$(Ba_{0.7}Ca_{0.3})TiO_3$ (BZT-BCT) stands out for its exceptionally high piezoelectric properties. Specifically, a piezoelectric coefficient d_{33} as high as 620 pC/N has been observed in polycrystalline $0.5Ba(Zr_{0.2}Ti_{0.8})O_3$-$0.5(Ba_{0.7}Ca_{0.3})TiO_3$ (50BZT-50BCT) [3]. Similar to $Pb(Zr,Ti)O_3$, the BZT-BCT solid solution crystallizes in three perovskite phases: paraelectric cubic ($Pm\bar{3}m$), ferroelectric rhombohedral ($R3m$), and ferroelectric tetragonal ($P4mm$) [3]. Recent reports suggest the presence of an intermediate orthorhombic phase ($Amm2$) within a narrow temperature and composition range [4–6]. For 50BZT-50BCT, this orthorhombic phase exists around room temperature within a temperature window narrower than 30 °C [6]. Most interestingly, it displays an anomalously low storage modulus as revealed by dynamic mechanical analysis [5].

Phenomenologically, the ultrahigh piezoelectric effect in 50BZT-50BCT is explained as due to the existence of a triple point close to room temperature [3]. From a microstructural perspective, this composition in its virgin state contains nanoscale ferroelectric domains that are believed to facilitate polarization rotation during electrical poling and to enhance piezoelectricity [7]. Even though ferroelectric domains are known to dictate the dielectric, piezoelectric, and ferroelectric properties of polar oxides, their original morphologies and even crystal symmetries often times cannot survive the electrical poling process, as recently demonstrated in $(K_{0.5}Na_{0.5})NbO_3$-based [8] and $(Bi_{1/2}Na_{1/2})TiO_3$-based [9] solid solutions. The effective polarization alignment and extensive phase transition during poling are cited as primary factors contributing to their excellent piezoelectric performances [8,9]. Presumably, the hierarchical domain structure observed in unpoled 50BZT-50BCT ceramics does not survive electrical poling either, as both 180° and non-180° domain switching have been observed in poled BZT-BCT solid solutions [10–13]. It should be noted that these x-ray diffraction investigations only focus on the ferroelastic/ferroelectric domain switching under high poling fields (>6.5 kV/cm), and most of the time are under *ex situ* conditions. Furthermore, no indication of any phase transition under electric field has been reported in this solid solution system. However, the coercive field of 50BZT-50BCT is extremely low (<2 kV/cm [3]), and several thermally induced phase transitions occur at temperatures close to room temperature [6]. To formulate a physics-based interpretation of the piezoelectricity in BZT-BCT, a detailed investigation of the domain polarization alignment at electric fields near the coercive field and possible phase transitions that occur during electrical poling is needed. For this, *in situ* transmission electron microscopy (TEM) under applied electric fields becomes critical.

A relevant issue related to piezoelectricity, especially in $BaTiO_3$-based compositions, is aging [14]. In a $(K_{0.5}Na_{0.5})NbO_3$-based polycrystalline ceramic, the piezoelectric response decays over time but can be recovered or even enhanced by a repoling [15]. It is therefore of fundamental importance to investigate the domain structure changes, and possible phase transitions, that occur during aging and repoling.

In this study, an electric field *in situ* TEM technique is used to monitor the polarization alignment process through domain switching and electric field-induced phase transitions due to the poling of virgin and aged polycrystalline 50BZT-50BCT. The observations in the TEM combined with electrical measurements and *in situ* x-ray diffraction experiments on bulk samples allow the elucidation of the physics origin of the piezoelectricity in 50BZT-50BCT. The experimental

*Corresponding author: xtan@iastate.edu

findings are supported by first-principles calculations on cubic, tetragonal, orthorhombic, and rhombohedral perovskite variants.

II. EXPERIMENTAL PROCEDURE

A. Sample preparation and characterization

The 50BZT-50BCT polycrystalline ceramic was prepared using a solid-state reaction method with details described in our previous reports [3,16]. The average grain size was determined to be 13.1 μm. A circular disk sample with sputtered silver films serving as electrodes was used for the bulk dielectric property measurements. These were carried out using a heating rate of 4 °C/min for a virgin state specimen, as well as the same specimen immediately after the room-temperature poling.

Electrodes were sputtered on to another pellet for *in situ* x-ray diffraction experiment. Cu-$K\alpha$ radiation was used at a 0.02° step size for the 2θ scan. The pseudocubic $(002)_C$, $(220)_C$, and $(222)_C$ peaks were recorded at a series of poling fields applied and maintained. The LHPM-Rietica software package was used for Rietveld refinement of the diffraction spectra.

The piezoelectric coefficient d_{33} and elastic compliance s_{33}^E under dc bias fields were determined with an impedance method that used bar-shaped specimens ($1 \times 1 \times 3$ mm^3). The dwell time for the measurement at each bias field was ~20 s. In order to avoid clamping effects of the resonance bars, thin silver leads were attached to the end faces with silver epoxy. The resonance and antiresonance frequencies of the virgin specimen were measured as a function of applied dc bias, which was increased from 0 to 8 kV/cm at 0.5 kV/cm increments. Also, the capacitance of a virgin disk sample was measured at 1 kHz under the same dc bias conditions. The piezoelectric coefficient d_{33} and elastic compliance constants s_{33}^D and s_{33}^E were then calculated. Another bar-shaped specimen was poled at room temperature with a dc field of 20 kV/cm from its virgin state. It was then allowed to age at room temperature for 5 days, and the d_{33} and s_{33}^E were measured during the repoling process following the same procedure described above.

For electric-field *in situ* TEM experiments, [8,9,17–19] disk specimens (3 mm in diameter) were prepared from as-sintered pellets through standard procedures, including grinding, cutting, dimpling, and ion milling. The dimpled disks were annealed at 200 °C for 2 h to minimize the residual stresses before Ar-ion milling to the point of electron transparency. *In situ* TEM experiments were carried out on a Phillips CM-30 microscope operated at 200 kV. After the first poling process from its virgin state, the same specimen was kept in the TEM for 4 days for the aging process and was then used for the repoling study. In the present work, the nominal electric field (the applied voltage divided by the electrode spacing) is cited for the *in situ* TEM results.

B. First-principles calculations

The first-principles calculations were performed using the density functional theory formalism, as implemented in the ABINIT software package [20,21]. Norm-conserving pseudopotentials were used in place of the all-electron ion potentials, and the exchange correlation energy was approximated using the Wu-Cohen formulation for the generalized gradient approximation [22]. The Brillouin zone was sampled using a Monkhorst-Pack $6 \times 6 \times 6$ k-point mesh [23], and the wave function was represented as a plane-wave expansion that was truncated at an energy of 80 Ry. Using these approximations, the atomic structures were optimized until the residual forces on the atoms were less than 5 meV/Å.

The composition of interest, with the formula $0.5Ba(Zr_{0.2}Ti_{0.8})O_3$-$0.5(Ba_{0.7}Ca_{0.3})TiO_3$, can be rewritten as $(Ba_{0.85}Ca_{0.15})(Ti_{0.90}Zr_{0.10})O_3$, which demonstrates that the compound can be imagined as a base compound $BaTiO_3$ codoped with of Ca^{2+} and Zr^{4+} at a ratio of 3:2. The virtual crystal approximation [24] was used to examine the compositions of $(Ba_{1-3x}Ca_{3x})(Ti_{1-2x}Zr_{2x})O_3$ for the range of $0.00 \leqslant x \leqslant 0.06$. When $x = 0.00$, the compound is pure $BaTiO_3$, and when $x = 0.05$, the composition is 50BZT-50BCT. For each composition, four phases were investigated: a paraelectric cubic phase and three ferroelectric phases, tetragonal, orthorhombic, and rhombohedral. The orthorhombic phase was modeled using a so-called $\sqrt{2}$ cell that is comprised of 10 atoms, but the other phases used the simple five-atom primitive cell. Each of the atomic structures and lattices were optimized under the constraint that they maintain their crystallographic symmetries.

III. RESULTS AND DISCUSSION

A. Structure-property evolution during initial poling

1. *In situ TEM observations*

The microstructural evolution under initial poling from the virgin state of polycrystalline 50BZT-50BCT is monitored in real-time on a representative grain along its [101] zone axis, as shown in Fig. 1. In the unpoled state [Fig. 1(a)], multiple domains are observed with the domain walls tracing along the ⟨001⟩, ⟨110⟩, and ⟨111⟩ directions, suggesting that they are very likely on {001} and {110} crystallographic planes. Most importantly, the hierarchical domain structure, which was reported as the distinct feature of this composition [7], is clearly observed in the upper middle part of Fig. 1(a). When the electric field reaches 2 kV/cm during initial poling [Fig. 1(b)], the hierarchical domain feature is disrupted, and also the domain wall density decreases. Multiple domains are still present with walls along two sets of {110} planes. A slight increase in the poling electric field to 2.5 kV/cm leads to a unique domain wall-free state [Fig. 1(c)], where the whole grain becomes a large single domain. However, such a single-domain state is not stable against higher poling fields. As exemplified in Fig. 1(d) at 4.25 kV/cm, two sets of {110} domain walls reappear even though the majority of the grain is still occupied by the large domain. The newly formed multidomain configuration becomes more apparent with the increase of domain wall density when the electric field further increases. As shown in Fig. 1(e)–1(g), at 5.75–10 kV/cm, new sets of domains are observed, and the domain wall density reaches its maximum at 8–10 kV/cm. Further increase in the poling field to 18 kV/cm leads to merging of lamellar domains into larger domains, but many domain

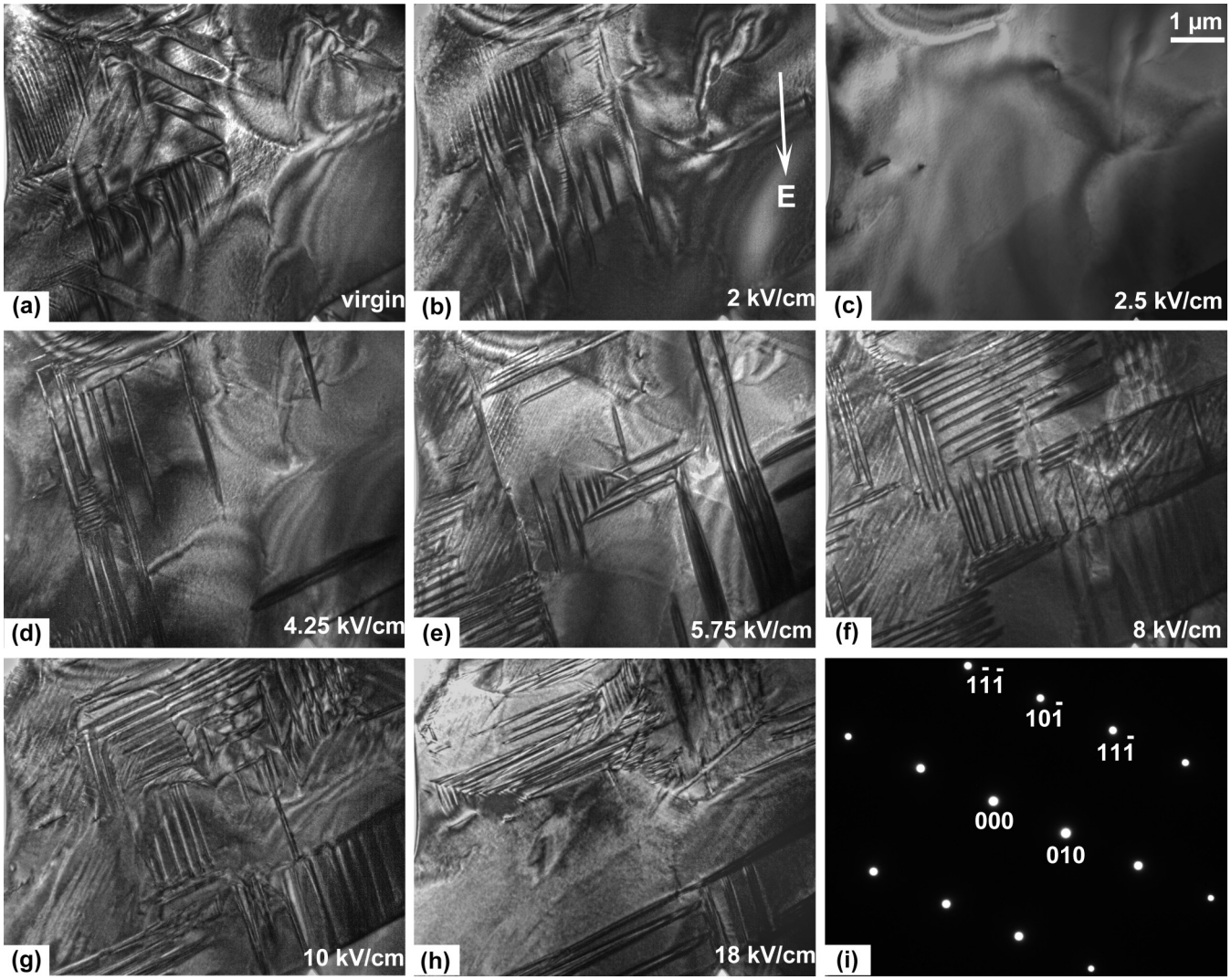

FIG. 1. *In situ* TEM observations of a grain along its [101] zone-axis in a polycrystalline 50BZT-50BCT specimen under electric fields during initial poling. Bright-field micrographs at (a) virgin state, (b) 2 kV/cm, (c) 2.5 kV/cm, (d) 4.25 kV/cm, (e) 5.75 kV/cm, (f) 8 kV/cm, (g) 10 kV/cm, and (h) 18 kV/cm are displayed. The direction of the poling field is indicated by the bright arrow in (b). The selected area diffraction pattern recorded at the virgin state is shown in (i). No apparent changes in the electron diffraction pattern are noticed during the initial poling process.

walls still persist. The corresponding selected area electron diffraction patterns during this initial poling process are also recorded. No noticeable changes to the fundamental diffraction spots and no appearances of any superlattice spots are observed [Fig. 1(i)].

Figure 2 shows another representative grain imaged along its [111] zone axis, where consistent results on the microstructure's response to initial poling are observed. In the virgin state prior to poling, the multidomain state with typical hierarchical domain structure is seen [Fig. 2(a)]. During the initial poling at 1 kV/cm [Fig. 2(b)], the domain morphology changes slightly. However, dramatic changes are observed when the electric field reaches 3.2 kV/cm; all of the domains disappear, and the whole grain transforms into a single-domain state [Fig. 2(c)]. Many lamellar domains with walls along two sets of {110} planes are developed upon further increasing the electric field [Fig. 2(d)]. In contrast to $(K_{0.5}Na_{0.5})NbO_3$-based [8] and $(Bi_{1/2}Na_{1/2})TiO_3$-based [9] ceramics, where poling-induced microstructure is largely preserved after the removal of the electric field, the multidomain configuration developed under high poling fields observed here in 50BZT-50BCT changes dramatically at zero field. As shown in Fig. 2(e), the long lamellar domains are disrupted by some short sets, but the multidomain state is preserved in this grain. Again, there is no observable change in the electron diffraction patterns during the poling process [Fig. 2(f)].

Our *in situ* TEM observations on 30 + grains reveal two scenarios for the domain configuration when the applied electric field is removed. When the grain is at the single-domain state, the removal of the poling electric field leads to the appearance of a few domains; but a good portion of the grain remains domain wall free. The single-domain state can be reproduced during an immediate repoling. When the applied field is high during the initial poling and the grain is in a multidomain state beyond the single-domain state, many domains are present in the grain after the removal of the field.

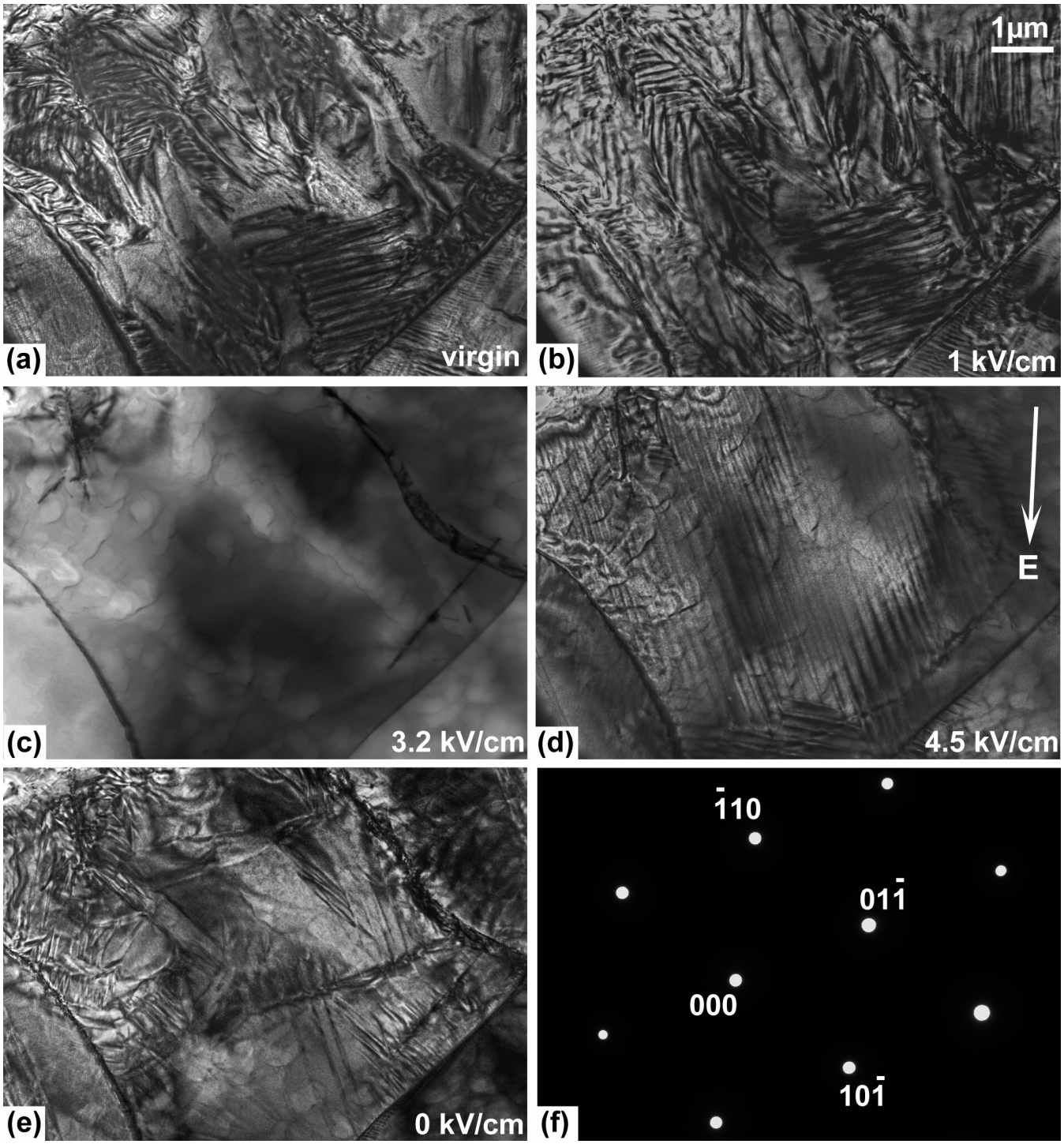

FIG. 2. *In situ* TEM observations of a grain along its [111] zone axis in a polycrystalline 50BZT-50BCT specimen under electric fields during initial poling. Bright-field micrographs at (a) virgin state, (b) 1 kV/cm, (c) 3.2 kV/cm, (d) 4.5 kV/cm, and (e) 0 kV/cm (the poling field is removed) are displayed. The direction of the poling field is indicated by the bright arrow in (d). The selected area diffraction pattern recorded at the virgin state is shown in (f). Again, no apparent changes in the electron diffraction pattern are noticed during initial poling.

The single-domain state is not observed upon an immediate repoling.

As noticed in Figs. 1 and 2, most of the domain walls in the multidomain state are found parallel to the {001} or {110} crystallographic planes. This information alone is not sufficient to reveal the crystal symmetry of these domains. For example, the {110} plane can be the 71° rhombohedral, 120° orthorhombic, and 90° tetragonal domain walls. Also, the {100} plane is permissible for 109° rhombohedral and 90° orthorhombic domain walls [8,25]. In our previous *in situ* TEM work [8,9], the crystal structure is inferred primarily from superlattice diffraction spots. Unfortunately, superlattice diffraction is not present in the current $BaTiO_3$-based composition, neither in its virgin state nor during poling under electric

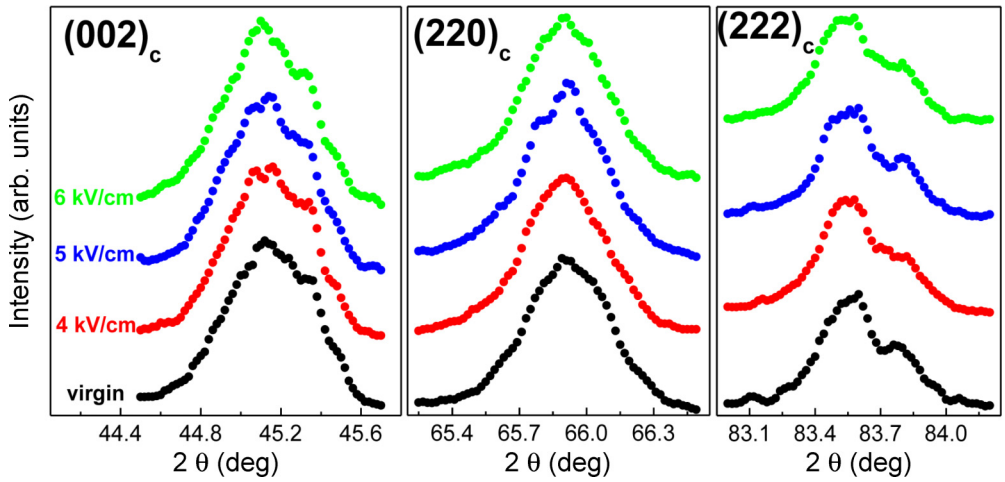

FIG. 3. (Color online) *In situ* x-ray diffraction analysis of a 50BZT-50BCT bulk sample during initial poling. The pseudocubic $(002)_C$, $(220)_C$, and $(222)_C$ reflections are recorded at the virgin state, as well as when poling fields of 4, 5, and 6 kV/cm are applied.

field. A separate detailed convergent beam electron diffraction analysis indicates that polycrystalline 50BZT-50BCT, at room temperature in its virgin state, is a two-phase mixture ($P4mm + R3m$) rather than a single $Amm2$ phase [26].

The presence of the single-domain state [Figs. 1(c) and 2(c)] at very low poling fields in a polycrystalline ceramic is quite unusual. This is repeatedly observed in all of the grains (>30) examined in several TEM specimens [27]. We speculate that the unique single-domain state in polycrystalline 50BZT-50BCT is in an orthorhombic phase based on the following facts. First, the virgin state of this composition at room temperature is a mixture of rhombohedral and tetragonal phases [26]. Second, the orthorhombic phase of this composition has an exceptionally low elastic modulus [5], much lower than those of $(Bi_{1/2}Na_{1/2})TiO_3$-based and $Pb(Zr,Ti)O_3$-based ceramics [28,29]. During electrical poling of polycrystalline ferroelectrics for piezoelectricity, the domain polarization alignment cannot be complete and many domains persist at grain boundary regions even at very high poling fields in order to accommodate the incompatible piezoelectric strain across the grain boundary [30]. The ultrasoft nature of the orthorhombic phase makes a single-domain state possible in polycrystalline 50BZT-50BCT for much reduced internal stresses.

2. *In situ x-ray diffraction analysis*

To experimentally verify the speculated phase transition from the mixed rhombohedral and tetragonal phases to the orthorhombic phase during poling, *in situ* x-ray diffraction experiments were carried out on a bulk sample, and the pseudocubic $(002)_C$, $(220)_C$, and $(222)_C$ peaks were monitored. The results are displayed in Fig. 3. In the virgin state, these convoluted peaks are not well resolved due to phase coexistence. The peak profiles start to change at 4 kV/cm during initial poling, as seen for both the $(002)_C$ and $(222)_C$ reflections. When the poling field reaches 5 kV/cm, peak splitting and intensity ratio change are observed on the $(002)_C$ and $(220)_C$ peaks. Additional changes are observed upon further increase in the poling electric field to 6 kV/cm.

A partial profile Rietveld refinement is performed on x-ray diffraction peaks from the virgin state and at 6 kV/cm. In the virgin state, the fractions for the $R3m$ and $P4mm$ phases are determined to be 75 and 25%, respectively, with $R_p = 3.48\%$ and $R_{wp} = 4.81\%$. At the poling field of 6 kV/cm, the best fit is found to be a mixture of $Amm2$ (66%) and $P4mm$ (34%), with $R_p = 2.96\%$ and $R_{wp} = 4.32\%$. Therefore, the *in situ* x-ray diffraction results support the proposed orthorhombic phase transition, even though a minor amount of the tetragonal phase is found to coexist. It is noted that the single-domain state is observed in the *in situ* TEM experiments under nominal fields mostly of 2–3 kV/cm, while the *in situ* x-ray diffraction tests recorded the orthorhombic phase between 4 and 6 kV/cm. The discrepancy in the field strength is due to several effects. First, the TEM specimen has a central perforation which intensifies the actual field in the area of interest [17]. The intensification ratio depends on the geometry of the perforation and the dielectric permittivity [31]. For a circular-shaped hole penetrating through the thickness of the 50BZT-50BCT ceramic, the actual field in the TEM observation area is roughly two times the nominal field. Second, the grain size in the 50BZT-50BCT ceramic is greater than 10 μm [32]. The response of individual grains to poling fields is likely to have an orientation dependence [33]. Further, *in situ* TEM experiments examine individual grains, while *in situ* x-ray tests collect information from many grains simultaneously. At 6 kV/cm, two-thirds of the grains are in the $Amm2$ structure (most likely domain wall-free according to *in situ* TEM observations). It should be pointed out that the refinement analysis here is rudimentary and qualitative, at best semiquantitative. More conclusive results are possible by refining whole diffraction patterns recorded from multiple specimens using high precision x-ray sources.

3. *Impact on properties*

Microstructural changes inevitably lead to alterations of properties. Figure 4 shows the temperature-dependent dielectric constant measured on a bulk sample in its virgin state, as well as after poling at 4 and 6 kV/cm, where the single-domain state in the orthorhombic phase is expected to develop. *In*

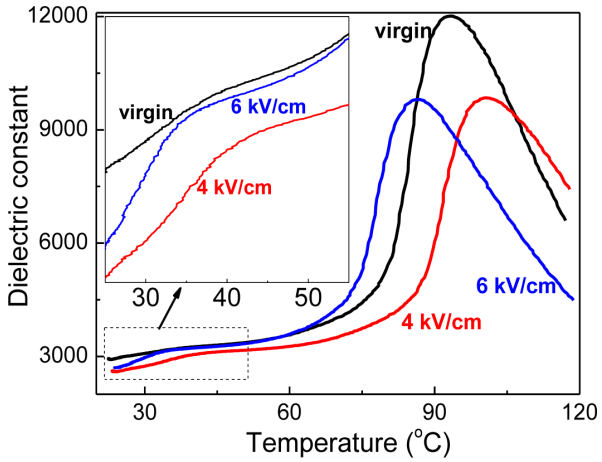

FIG. 4. (Color online) Temperature dependence of the dielectric constant measured at 10 kHz during heating on a bulk sample of 50BZT-50BCT in its virgin state, as well as after poling. The measurements were made with no dc bias.

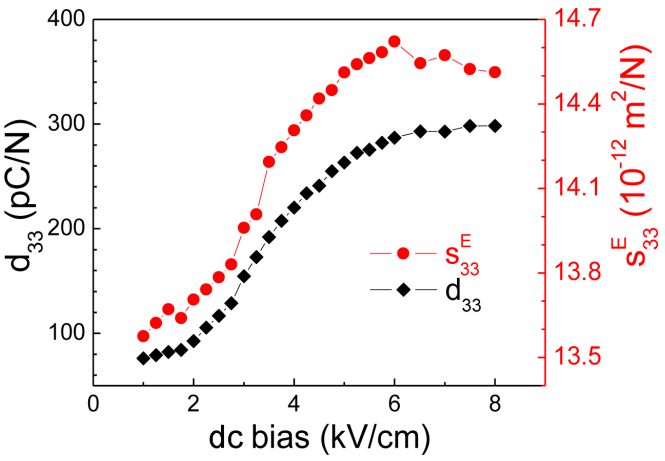

FIG. 5. (Color online) *In situ* measurements of the piezoelectric coefficient d_{33} and the elastic compliance constant s_{33}^E, as a function of dc bias field on a bulk sample of 50BZT-50BCT. Error bars are less than the symbol size and are not shown. The dc bias field serves as the poling field to develop piezoelectricity.

situ TEM experiments reveal that large portions of the grains remain domain wall free after the poling field is removed from the single-domain state. Such changes in microstructure are reflected in the dielectric behavior, especially around room temperature. As highlighted in the inset, the slope change on the curve from virgin state is barely seen. After poling, the change in slope at around 35 °C becomes abundantly apparent. This appears to be consistent with the fact that polycrystalline 50BZT-50BCT is a mixture of rhombohedral and tetragonal phases in the virgin state; the transition to the tetragonal phase during heating is hence gradual and hardly detected by the change in dielectric constant. After poling to the single-domain state at 4 or 6 kV/cm, the orthorhombic phase is largely preserved when the field is removed; a sharper transition ensues during the subsequent heating.

Note that the Curie temperature T_C changes with the poling field. In its virgin state, T_C is 93 °C. After being poled at 4 kV/cm, it shifts to a higher temperature of 101 °C. T_C drops to 87 °C after poling at 6 kV/cm. A striking shift of 14 °C is observed here. The impact of electrical poling on Curie temperature has been reported previously in various perovskite compounds and is attributed to the poling-induced domain configuration [34–36].

In order to directly correlate electromechanical properties from bulk samples with *in situ* TEM and x-ray diffraction structural studies, measurements of the piezoelectric coefficient d_{33} and the elastic compliance constant s_{33}^E are carried out on a virgin sample under a series of dc bias fields, which serve as the poling fields. The results are shown in Fig. 5. The piezoelectric coefficient is observed to increase slowly before 2 kV/cm and then displays a fast increase at 3–6 kV/cm, followed by a slow increase again at 6–8 kV/cm. The elastic compliance constant displays a discontinuous jump around 3 kV/cm, then keeps increasing and reaches its maximum value at 6 kV/cm. A decreasing trend appears at 6–8 kV/cm. The macroscopic properties d_{33} and s_{33}^E measured *in situ* with dc bias fields correlate well with the *in situ* TEM results. At very low poling fields, the initial domain configuration changes slightly and the polycrystalline 50BZT-50BCT is still largely unpoled. Under the poling field of ~3 kV/cm, the unique single-domain state in the orthorhombic phase starts to form. The exceptional softness of the orthorhombic phase contributes to the abrupt increase in s_{33}^E. The fast increase in d_{33} appears to suggest a major contribution from this elastic softening. At higher poling fields (>6 kV/cm), another phase transition occurs, and multidomains in a different phase are formed. Correspondingly, s_{33}^E decreases, and the increase in d_{33} slows down.

B. Structure-property evolution during repoling

1. *In situ TEM observations*

The same grain shown in Fig. 2 is examined again under electric field after the specimen is left in the TEM column for 4 days. The microstructural evolution during the repoling process is displayed in Fig. 6. Figure 6(a) shows the aged state prior to repoling; the multidomain state is still present with almost all domain walls aligned along three $\langle 1\bar{1}0\rangle$ directions. However, by comparing to the domain morphology in Fig. 2(e), we see that many new domains are formed during aging. At the repoling field of 2.5 kV/cm, the grain is almost completely occupied by a major set of $(01\bar{1})$ domain walls [Fig. 6(b)]. These lamellar domains entirely disappear at 3.75 kV/cm, where a single-domain state is reached again, shown in Fig. 6(c). Further increasing the repoling field to 5.5 kV/cm triggers the formation of many lamellar domains with walls along $(01\bar{1})$ and $(1\bar{1}0)$ planes [Fig. 6(d)]. Also, some $[10\bar{1}]$-aligned domain traces emerge. These $[10\bar{1}]$-aligned domain walls become more apparent with the development of a cluster of thin and long lamellar domains in the upper left part of Fig. 6(e). In addition, a new feature in a lenticular shape with long axis roughly along the $[\bar{1}2\bar{1}]$ direction is also noticed at 6.25 kV/cm. The complicated domain morphology keeps evolving as the repoling field increases. At 8 kV/cm, many domain walls disappear, with the remaining ones primarily on two sets of {110}, as shown in Fig. 6(f).

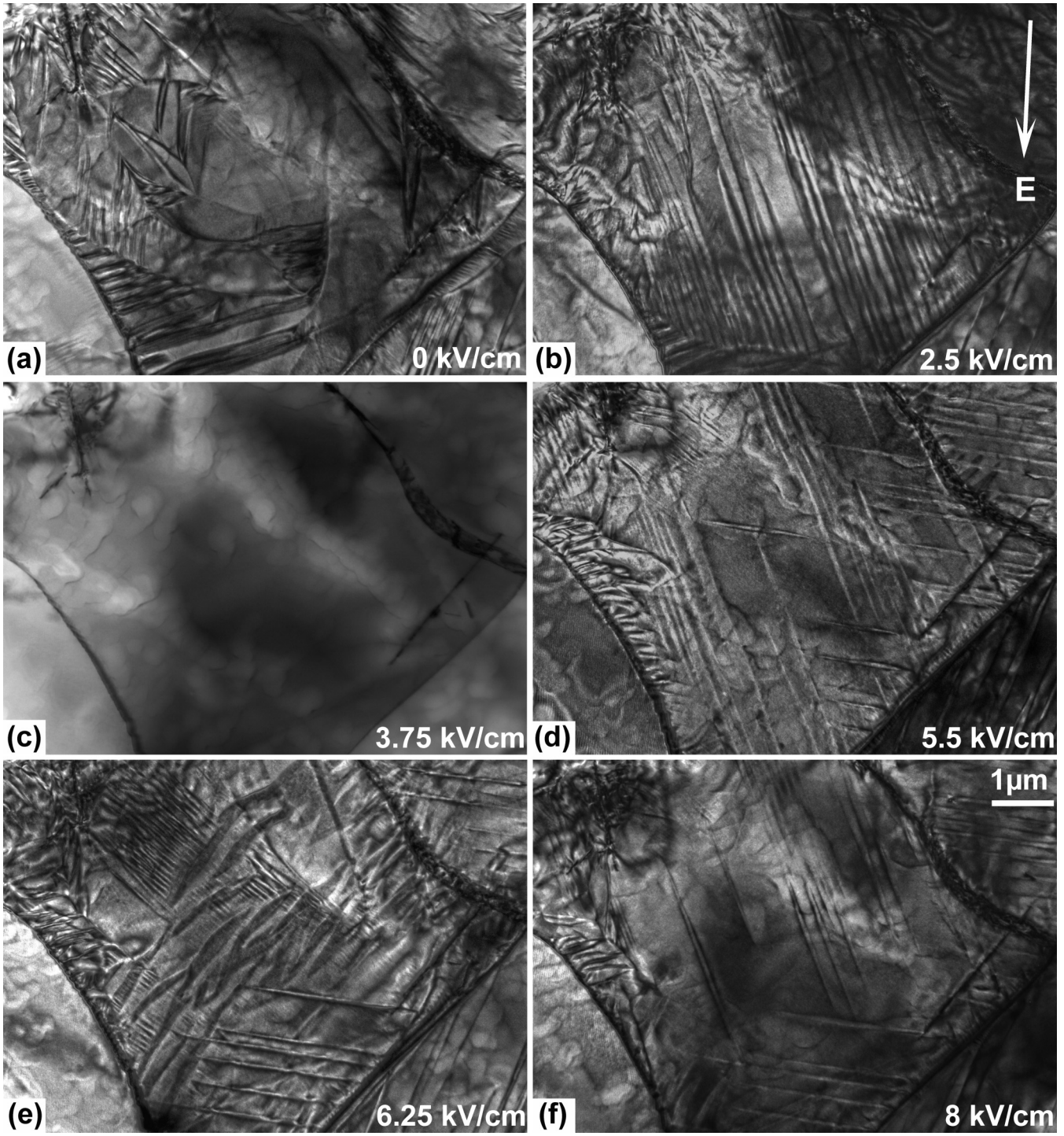

FIG. 6. *In situ* TEM observations on the same grain shown in Fig. 2 after the specimen is aged in the TEM column for 4 days. Bright-field micrographs at (a) 0 kV/cm, (b) 2.5 kV/cm, (c) 3.75 kV/cm, (d) 5.5 kV/cm, (e) 6.25 kV/cm, and (f) 8 kV/cm are displayed to reveal the microstructural change during the repoling process. The direction of the repoling field is indicated by the bright arrow in (b).

It is interesting that the single-domain state reappears during the repoling process only after the specimen is aged. As noted in Sec. III A 1, the single-domain state cannot be reached by repoling immediately after the multidomain configuration is formed during the initial poling at high fields (>6 kV/cm). Therefore, to some extent, aging seems to resume the original rhombohedral and tetragonal phases in polycrystalline 50BZT-50BCT. This makes it possible for an electric-field-induced single-domained orthorhombic phase to appear during repoling.

2. *Impact on properties*

The d_{33} and s_{33}^{E} were also measured during the repoling process on a bulk sample that was poled with a dc field of 20 kV/cm and then aged for 5 days. As can be seen in Fig. 7,

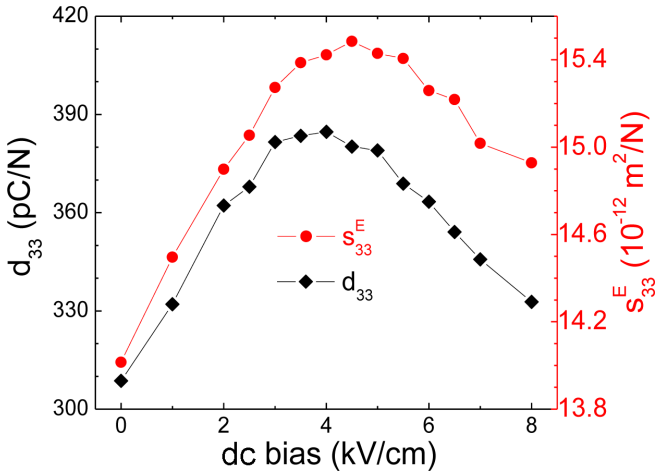

FIG. 7. (Color online) *In situ* measurements of the piezoelectric coefficient d_{33} and elastic compliance constant s_{33}^E, as a function of dc bias field after the specimen is aged at room temperature for 5 days. Error bars are less than the symbol size and are not shown. The dc bias field serves as the repoling field.

similar trends are observed for d_{33} and s_{33}^E; they both increase first and then decrease. An enhancement of ~20% in d_{33} to a value of 385 pC/N is achieved at the repoling field of 4 kV/cm. At the same time, s_{33}^E reaches a peak value of 15.5 pm^2/N at 4.5 kV/cm, corresponding to a 10% increase from the aged state. It is believed that the elastic softening associated with the formation of the single-domain orthorhombic phase contributes to the piezoelectricity enhancement during the repoling process.

C. Structure and energy from first-principles calculations

To better understand the relationship between the phases, first-principles calculations are performed on $(Ba_{1-3x}Ca_{3x})(Ti_{1-2x}Zr_{2x})O_3$, where x ranges from 0.00 to 0.06. The lattice parameters of the four phases for each composition are shown in Fig. 8. The base compound $BaTiO_3$ ($x = 0.00$) has lattice parameters that are consistent with the experimental and theoretical values reported in the literature [37]. As Ca^{2+} and Zr^{4+} concentrations are increased, on A- and B-sites respectively, the lattice parameters begin to approach a common value, and when $x = 0.05$, which is the 50BZT-50BCT composition studied here, a uniform cubic structure is predicted. Moreover, the relative energies for this unique composition were also calculated and are compared in Fig. 9, using the energy for the relaxed cubic structure as the reference energy. It is evident that all phases in 50BZT-50BCT are equienergetic.

It is not anticipated that these results predicted in small unit cells (5–10 atoms) will mimic the observations from large multidomain or multigrain experiments. However, they validate the uniqueness of the 50BZT-50BCT composition. It represents a point where these four phases are energetically and structurally similar and therefore coexist, which allows for the enhanced electromechanical properties observed in the experiment. In this capacity, the first-principles calculations provide validation of the observed structural instability and

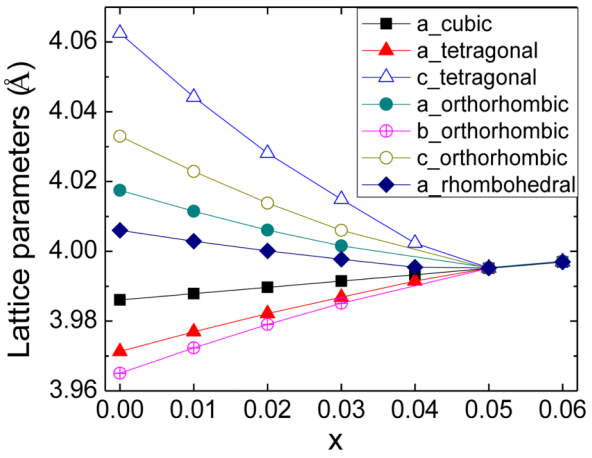

FIG. 8. (Color online) Lattice parameters of the cubic, tetragonal, orthorhombic, and rhombohedral phases in $(Ba_{1-3x}Ca_{3x})(Ti_{1-2x}Zr_{2x})O_3$ from first-principles calculations. The composition $x = 0.05$ corresponds to the experimentally investigated 50BZT-50BCT.

the ease for the system to undergo phase transitions at low electric fields in this composition. In particular, it explains why room-temperature aging can be used to modify the domain structures.

D. Discussion

Many factors contribute to a material having a large piezoelectric response, such as the structural instability, domain wall motion, a low-symmetry phase, and elastic softening [3,8,9,38,39]. We believe the structural instability, as manifested by the easy and close-to-room-temperature phase transition, and the elastic softening associated with the field-induced domain-free orthorhombic phase are the two primary factors in polycrystalline 50BZT-50BCT.

Structural instabilities exist at polymorphic phase boundary (PPB) or morphotropic phase boundary (MPB) compositions [39], and as a result, there is a significant enhancement of the piezoelectricity [8,9]. Multiple perovskite variants

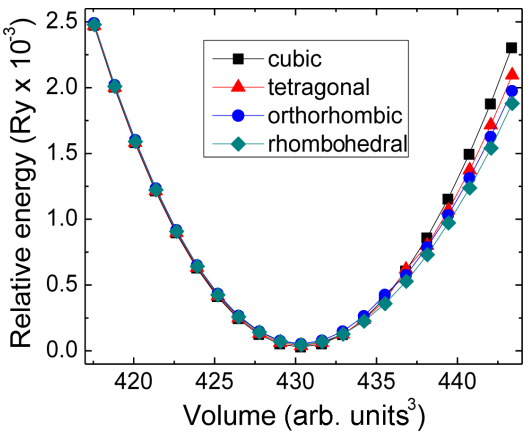

FIG. 9. (Color online) Relative energies for the four phases of 50BZT-50BCT. The energy of the cubic phase is arbitrarily defined as the energy zero.

must have comparable free energies at these PPB or MPB compositions, implying that the microstructure will be highly responsive to poling fields. The polycrystalline 50BZT-50BCT in this study displays close-to-room-temperature transitions: two are ferroelectric-ferroelectric transitions [5,6], and another is the ferroelectric-paraelectric transition at 93 °C (Fig. 4). Consequently, the microstructure of the ceramic responds to the poling field by domain switching starting at a very low field, then the disappearance of all domain walls and a phase transition to the orthorhombic phase, then reappearance of multiple domains and another phase transition. Evidence for the structural instabilities in 50BZT-50BCT is further provided by the first-principles calculations, where the four phases are found energetically and structurally similar and hence can easily transform to and from each other (Figs. 8 and 9).

Generally speaking, low polarization anisotropy and lattice softening go hand in hand, both contributing to the high piezoelectric response [3]. Theoretical studies have shown that elastic softening can significantly enhance the piezoelectric response in perovskite-type oxides and also wurtzite structured alloys [40,41]. In its virgin state, polycrystalline 50BZT-50BCT has an elastic compliance constant (s_{33}^E), with a peak around room temperature, which corresponds to the anomalously high piezoelectric property [16]. In the present study, measurements of s_{33}^E under dc bias fields, which simulate the initial poling and the repoling process, elastic softening is also observed, as shown in Figs. 5 and 7. Correspondingly, the microstructure adopts the single-domain state with an orthorhombic structure. The correlation of enhanced piezoelectricity with high elastic compliance constant has been widely observed in perovskite-structured piezoelectrics [16,38,40,42–44]. Elastic softening is believed to effectively relax the lattice of the crystal and facilitate the structural instability when external stimuli (temperature, stress, and electric field) are applied. As a consequence, optimized piezoelectric properties are always accompanied with the peak value of elastic compliance constant (or the minimum value of elastic modulus). This is the case here for 50BZT-50BCT; this is the case for lead-based [38,43,44] and lead-free solid solutions [16,42]; and this is the case, even for the simple compound $BaTiO_3$ [1,45].

IV. CONCLUSIONS

In conclusion, the development of piezoelectricity in polycrystalline 50BZT-50BCT due to initial poling and repoling is investigated, and the microstructural origins are identified. First-principles calculations indicate that this composition is unique as its rhombohedral, orthorhombic, tetragonal, and cubic variant phases are almost indistinguishable in terms of lattice parameters and energetics. As a consequence, this ceramic is extremely responsive to the poling fields. In addition to extensive domain polarization alignment activities, a unique single-domain state is observed with poling fields in the range of 3–6 kV/cm. The single-domain state is believed to be in the orthorhombic phase, which has an exceptionally low elastic modulus. The structural instability and the elastic softening during initial poling and repoling are suggested to be the primary contributing factors to the excellent piezoelectricity in this newly developed $BaTiO_3$-based lead-free ceramic.

ACKNOWLEDGMENTS

The National Science Foundation, through Grant No. DMR-1037898, supported this work.

[1] B. Jaffe, W. R. Cook, and H. Jaffe, *Piezoelectric Ceramics* (Academic Press, London, 1971).
[2] S. J. Zhang, R. Xia, and T. R. Shrout, J. Electroceram. **19**, 251 (2007).
[3] W. Liu and X. Ren, Phys. Rev. Lett. **103**, 257602 (2009).
[4] Y. Tian, L. Wei, X. Chao, Z. Liu, and Z. Yang, J. Am. Ceram. Soc. **96**, 496 (2013).
[5] D. Damjanovic, A. Biancoli, L. Batooli, A. Vahabzadeh, and J. Trodahl, Appl. Phys. Lett. **100**, 192907 (2012).
[6] D. S. Keeble, F. Benabdallah, P. A. Thomas, M. Maglione, and J. Kreisel, Appl. Phys. Lett. **102**, 092903 (2013).
[7] J. Gao, D. Xue, Y. Wang, D. Wang, L. Zhang, H. Wu, S. Guo, H. Bao, C. Zhou, W. Liu, S. Hou, G. Xiao, and X. Ren, Appl. Phys. Lett. **99**, 092901 (2011).
[8] H. Z. Guo, S. Zhang, S. P. Beckman, and X. Tan, J. Appl. Phys. **114**, 154102 (2013).
[9] C. Ma, H. Z. Guo, S. P. Beckman, and X. Tan, Phys. Rev. Lett. **109**, 107602 (2012).
[10] M. C. Ehmke, S. N. Ehrlich, J. E. Blendell, and K. J. Bowman, J. Appl. Phys. **111**, 124110 (2012).
[11] M. C. Ehmke, J. Daniels, J. Glaum, M. Hoffman, J. E. Blendell, and K. J. Bowman, J. Appl. Phys. **112**, 114108 (2012).
[12] M. C. Ehmke, J. Glaum, M. Hoffman, J. E. Blendell, and K. J. Bowman, J. Am. Ceram. Soc. **96**, 3805 (2013).
[13] M. C. Ehmke, J. Glaum, M. Hoffman, J. E. Blendell, and K. J. Bowman, J. Am. Ceram. Soc. **96**, 2913 (2013).
[14] L. X. Zhang and X. Ren, Phys. Rev. B **73**, 094121 (2006).
[15] K. Wang and J. F. Li, Adv. Funct. Mater. **20**, 1924 (2010).
[16] D. Xue, Y. Zhou, H. Bao, C. Zhou, J. Gao, and X. Ren, J. Appl. Phys. **109**, 054110 (2011).
[17] X. Tan, H. He, and J. K. Shang, J. Mater. Res. **20**, 1641 (2005).
[18] H. Z. Guo, C. Ma, X. M. Liu, and X. Tan, Appl. Phys. Lett. **102**, 092902 (2013).
[19] X. Tan, Z. Xu, J. K. Shang, and P. Han, Appl. Phys. Lett. **77**, 1529 (2000).
[20] X. Gonze, B. Amadon, P. M. Anglade, J. M. Beuken, F. Bottin, P. Boulanger, F. Bruneval, D. Caliste, R. Caracas, M. Côté, T. Deutsch, L. Genovese, Ph. Ghosez, M. Giantomassi, S. Goedecker, D. R. Hamann, P. Hermet, F. Jollet, G. Jomard, S. Leroux *et al.*, Comput. Phys. Commun. **180**, 2582 (2009).
[21] X. Gonze, G. M. Rignanese, M. Verstraete, J. M. Beuken, Y. Pouillon, R. Caracas, F. Jollet, M. Torrent, G. Zerah, M. Mikami, P. Ghosez, M. Veithen, J. Y. Raty, V. Olevano, F. Bruneval, L. Reining, R. Godby, G. Onida, D. R. Hamann, and D. C. Allan, Z. Kristallogr. **220**, 558 (2005).

[22] Z. G. Wu and R. E. Cohen, Phys. Rev. B **73**, 235116 (2006).
[23] H. J. Monkhorst and J. D. Pack, Phys. Rev. B **13**, 5188 (1976).
[24] Ph. Ghosez, D. Desquesnes, X. Gonze, and K. M. Rabe, AIP Conf. Proc. **535**, 102 (2000).
[25] D. I. Woodward, J. Knudsen, and I. M. Reaney, Phys. Rev. B **72**, 104110 (2005).
[26] J. Gao, L. Zhang, D. Xue, T. Kimoto, M. Song, L. Zhong, and X. Ren, J. Appl. Phys. **115**, 054108 (2014).
[27] H. Z. Guo, C. Zhou, X. Ren, and X. Tan, Phys. Rev. B **89**, 100104(R) (2014).
[28] Y. Yao, Z. Sun, Y. Ji, Y. Yang, X. Tan, and X. Ren, Sci. Technol. Adv. Mater. **14**, 035008 (2013).
[29] S. E. Young, H. Z. Guo, C. Ma, M. R. Kessler, and X. Tan, J. Therm. Anal. Calorim. **115**, 587 (2014).
[30] X. Tan, C. Ma, J. Frederick, S. Beckman, and K. G. Webber, J. Am. Ceram. Soc. **94**, 4091 (2011).
[31] R. M. McMeeking, J. Appl. Math. Phys. **40**, 615 (1989).
[32] J. Wu, D. Xiao, W. Wu, Q. Chen, J. Zhu, Z. Yang, and J. Wang, J. Eur. Ceram. Soc. **32**, 891 (2012).
[33] J. Hirohashi, K. Yamada, H. Kamio, M. Uchida, and S. Shichijyo, J. Appl. Phys. **98**, 034107 (2005).
[34] R. Aoyagi, A. Takeda, M. Iwata, M. Maeda, T. Nishida, and T. Shiosaki, Jpn. J. Appl. Phys. **47**, 7689 (2008).
[35] B. S. Semwal and P. K. Sharma, Can. J. Phys. **51**, 1874 (1973).
[36] G. Shirane, E. Sawaguchi, and Y. Takagi, Phys. Rev. **84**, 476 (1951).
[37] J. J. Wang, F. Y. Meng, X. Q. Ma, M. X. Xu, and L. Q. Chen, J. Appl. Phys. **108**, 034107 (2010).
[38] S. J. Zhang and F. Li, J. Appl. Phys. **111**, 031301 (2012).
[39] D. Damjanovic, IEEE Trans. Ultrason. Ferroelectr. Freq. Control **56**, 1574 (2009).
[40] M. Iwata, H. Orihara, and Y. Ishibashi, Ferroelectrics **266**, 57 (2002).
[41] F. Tasnádi, B. Alling, C. Höglund, G. Wingqvist, J. Birch, L. Hultman, and I. A. Abrikosov, Phys. Rev. Lett. **104**, 137601 (2010).
[42] S. J. Zhang, R. Xia, and T. R. Shrout, J. Appl. Phys. **100**, 104108 (2006).
[43] A. K. Singh, S. K. Mishra, Ragini, D. Pandey, S. Yoon, S. Baik, and N. Shin, Appl. Phys. Lett. **92**, 022910 (2008).
[44] E. H. Kisi, R. O. Piltz, J. S. Forrester, and C. J. Howard, J. Phys.: Condens. Matter **15**, 3631 (2003).
[45] P. Zheng, J. L. Zhang, Y. Q. Tan, and C. L. Wang, Acta Mater. **60**, 5022 (2012).